Atomic-Scale Characterization of Oxide Interfaces and Superlattices Using Scanning Transmission Electron Microscopy

Chapter · August 2017

DOI: 10.1016/B978-0-12-409547-2.12877-X

2 authors, including:

Steven Richard Spurgeon
Pacific Northwest National Laboratory
76 PUBLICATIONS **280** CITATIONS

SEE PROFILE

Atomic-Scale Characterization of Oxide Interfaces and Superlattices Using Scanning Transmission Electron Microscopy

SR Spurgeon and SA Chambers, Pacific Northwest National Laboratory, Richland, WA, United States

Introduction

Over the past several decades, scanning transmission electron microscopy (STEM) has emerged as one of the most robust and versatile platforms for materials characterization.[1–11] Augmented with advanced aberration-correctors, modern electron microscopes enable the simultaneous analysis of crystallography, defects, chemistry, and composition at the atomic-scale. Thin-film oxide heterostructures, which possess intimate coupling among spin, lattice, and orbital degrees of freedom, represent ideal structures for leveraging the power of STEM-based techniques. Precision deposition methods, such as molecular beam epitaxy (MBE) and pulsed laser deposition (PLD), permit the integration of systems with disparate chemical, electronic, and magnetic properties, unlocking emergent phenomena at interfaces.[12–16] Since these structures are typically synthesized in conditions far from equilibrium, it is often difficult to predict their structure and properties *a priori*, necessitating detailed investigation including local STEM probes. The information provided by STEM imaging and spectroscopy can refine first-principles calculations that can in turn be distilled into improved models for the behavior of these novel systems.

STEM techniques, encompassing imaging and diffraction, as well as electron energy loss (STEM-EELS) and energy-dispersive X-ray (STEM-EDS) spectroscopies, are uniquely suited to the analysis of oxide heterostructures and interfaces. These materials generally possess large lattice parameters that are compatible with larger electron probes and their associated higher beam currents, providing enhanced spectroscopic signals. Conveniently, the threshold for beam damage in oxides is much higher than for many other systems,[17] permitting exquisite visualization without significant damage. In addition, the transition metal cations in oxides generally possess sizable X-ray fluorescence yields that facilitate rapid EDS composition mapping. Furthermore, investigations using other X-ray core-level spectroscopies[18] have established a rich theoretical framework to interpret EELS fine structure; experimental efforts are supported by *ab initio* calculations of electronic structure,[19–21] as well as multislice-based image and ionization map simulations.[22–25]

Our understanding of many oxide systems, encompassing applications ranging from multiferroics to spintronics, has been greatly shaped by STEM characterization.[26–28] Using STEM-EELS it is possible to visualize interfacial mixing, which is a candidate mechanism for resolving the polar catastrophe at polar/ nonpolar interfaces.[3,29,30] Electronic reconstructions at interfaces can also be directly measured,[31–33] informing our understanding of two-dimensional electron gas (2DEG) formation. However, while advances in instrumentation have undoubtedly made atomic-scale mapping more commonplace, the interpretation of data is still fraught with challenges. Complex beam–specimen interactions influence STEM-EDS[4,22,23,34–39] and STEM-EELS[22,36,40–43] mapping, leading to delocalization and channeling effects that can complicate interface analysis.[44,45] As more robust and complex modeling packages have been developed, significant strides have been made toward better quantification,[22,34,46] further elevating these techniques as central tools for materials analysis.

In this article we review results from our investigations of key oxide interfaces and superlattices. In particular, we emphasize the high spatial resolution and direct nature of STEM characterization, in contrast to spatially averaged X-ray and ion scattering techniques. In the "**Cation Intermixing and Electronic Defects in LCO/STO Superlattices**" section we discuss how STEM-EELS may be used to probe cation intermixing and potential sources of interfacial conductivity in model $LaCrO_3$ (LCO)/$SrTiO_3$ (STO) superlattices. The "**Interfacial Phase Mapping of LSMO/PZT Magnetoelectric Heterostructures**" section describes an approach to map interfacial phases formed by screening of bound charge in magnetoelectric $La_{1-x}Sr_xMnO_3$ (LSMO)/$PbZr_xTi_{1-x}O_3$ (PZT) heterostructures; this study highlights how density functional theory (DFT) calculations may be used to interpret EELS fine structure measurements. The "**Interface Characterization of Fe_2O_3/Cr_2O_3 Heterostructures for Photocatalysis**" section shows how information from both STEM-EELS and STEM-EDS may be combined to improve the design of high-quality Fe_2O_3/Cr_2O_3 superlattices for photoelectrochemical water splitting. Finally, the "**Challenges to Quantification of Atomic-Scale STEM-EDS Maps**" section addresses commonly overlooked limitations of STEM-EDS mapping, illustrating the dramatic effect of sample

preparation on quantification of interfacial mixing. These examples demonstrate the breadth, depth, and complexity of STEM analysis techniques, as well as the unique insight they provide into the properties of oxide superlattices and interfaces.

Cation Intermixing and Electronic Defects in LCO/STO Superlattices

Perovskite oxides are among the most ubiquitous functional materials, owing to their high degree of structural compatibility across different stoichiometries and the wide range of emergent properties at their surfaces and interfaces.[47,48] Extensive work has focused on polar/nonpolar interfaces, particularly in the archetypal $LaAlO_3$ (LAO)/STO system,[49] but models frequently assume a perfectly abrupt interface across which electron transfer occurs. However, previous studies[29,50,51] have found that intermixing is quite common in these materials, indicating that extrinsic defects may play a more important role in mediating interface conductivity than commonly thought. The success of this past work suggests that oxide LCO/STO superlattices consisting of asymmetrically terminated layers may also possess a bulk-like built-in potential gradient.[52,53] While this system is promising for separation of photoexcited electron–hole pairs, the effects of intermixing and cation defects on the potential are poorly described. The most rigorous characterization approaches use Rutherford backscattering (RBS), X-ray absorption spectroscopy, and X-ray photoelectron spectroscopy (XPS), which are either volume-averaged or surface-limited; in contrast, STEM-EELS combines fine structure information and high spatial resolution to locally measure intermixing and electronic defects.[3] A correlative approach, leveraging multiple techniques, is essential to compose more accurate and realistic interface models.

We have examined MBE-grown LCO/STO superlattices on $(LaAlO_3)_{0.3}$ $(Sr_2AlTaO_6)_{0.7}$ (LSAT) (001) substrates.[54] While our previous STEM measurements confirm a polarization induced by the alternation of positively charged $[TiO_2]^0$ | $[LaO]^+$ and negatively charged $[CrO_2]^-$ | $[SrO]^0$ interfaces, we also find evidence for an unexpected conductivity in our samples.[52] To probe the origin of this conductivity, we have conducted extensive STEM-EELS mapping. Fig. 1A shows cross-sectional high-angle annular dark field imaging (STEM-HAADF), which reveals a high-quality superlattice consisting of $[6\ STO/3\ LCO]_{\times 10}$ units. We observe that the film is coherent and epitaxial, with no visible misfit dislocations or secondary phases. Fig. 1B shows a composite STEM-EELS map of the integrated La $M_{4,5}$, Cr $L_{2,3}$ and Ti $L_{2,3}$ signals, highlighting the asymmetric termination at each block of the superlattice. Fig. 1C and D shows line profiles averaged in the film plane for the integrated Ti $L_{2,3}$ edge intensity and Ti L_3 $t_{2g}-e_g$ crystal field splitting, respectively; the latter may be used to investigate potential valence changes, since the transition metal white-lines result from excitations from spin–orbit split $2p_{3/2}$ and $2p_{1/2}$ states to available $3d$ band states.[55] Similarly, Fig. 1E and F show line profiles averaged in the film plane for the integrated Cr $L_{2,3}$ edge intensity and O K – Cr L_3 edge energy loss separation, respectively. These spectra exhibit measurable Ti and Cr signals in all the layers of the superlattice, although the degree of Cr intermixing is less than that of Ti. We have previously observed sizable Ti outdiffusion in LCO/STO bilayers, which we believe improves the thermodynamic stability of the interface.[56]

In light of this cation intermixing, we next consider potential valence changes and defects associated with this behavior. White-line ratios, though commonly used to estimate local valence, are challenging to compare to results from other groups, owing to subjective differences in background subtraction as well as position-sensitive effects.[40] Instead, we fit the energy loss separation of the Ti L_3 and L_2 edges at each pixel of chemical map, generating the integrated line profile shown in Fig. 1D. We observe an average value across the superlattice that falls within the literature range for a Ti^{4+} state; however, the overall profile is tilted toward a slight Ti valence reduction at the film surface, suggesting possible accumulation of excess La. The white-line ratio method is similarly difficult to apply to the Cr $L_{2,3}$ edge because of its overlap with the O K continuum, so we instead consider the Cr L_3 to O K edge separation, which is a known indicator of local valence.[57,58] We again observe that this quantity falls within the expected range of values for a Cr^{3+} state; however, we observe a slight reduction near the interfaces with STO, indicating the possible compensation of Ti^{4+} cations in the nearby STO layers. A comparison to DFT calculations for various defect scenarios shows that excess La can give rise to additional carriers in the STO. Cr substitution for Ti in the STO layer can lead to oxygen vacancy formation due to the instability of octahedrally coordinated Cr^{4+}, suppressing interfacial hole formation and preserving the built-in potential across the superlattice.

Taken together, our results underscore the importance of correlative high-resolution chemical and composition analysis alongside data from volume-averaged techniques. STEM-EELS reveals a "real" interface that stands in stark contrast to the often assumed perfectly abrupt models typically employed in theoretical calculations. The parameters extracted from these measurements can serve as an input for first-principles calculations, refining our understanding of the complex interplay between structure and defects.

Interfacial Phase Mapping Of LSMO/PZT Magnetoelectric Heterostructures

Manganite-based heterostructures represent one of the most widely studied oxide systems because of their intimate coupling among structure, electronic, and magnetic order, which form the basis for spintronic devices.[59–62] Early reports of colossal magnetoresistance (CMR)[63,64] triggered extensive synthesis and characterization efforts throughout the 1990s and early 2000s. The magnetoelectric effect, which heretofore had only been identified in a handful of monolithic compounds (e.g., Cr_2O_3[65,66] and thin-film $BiFeO_3$ (BFO)[67]), was expanded to encompass a new class of composite magnetoelectrics engineered to couple the

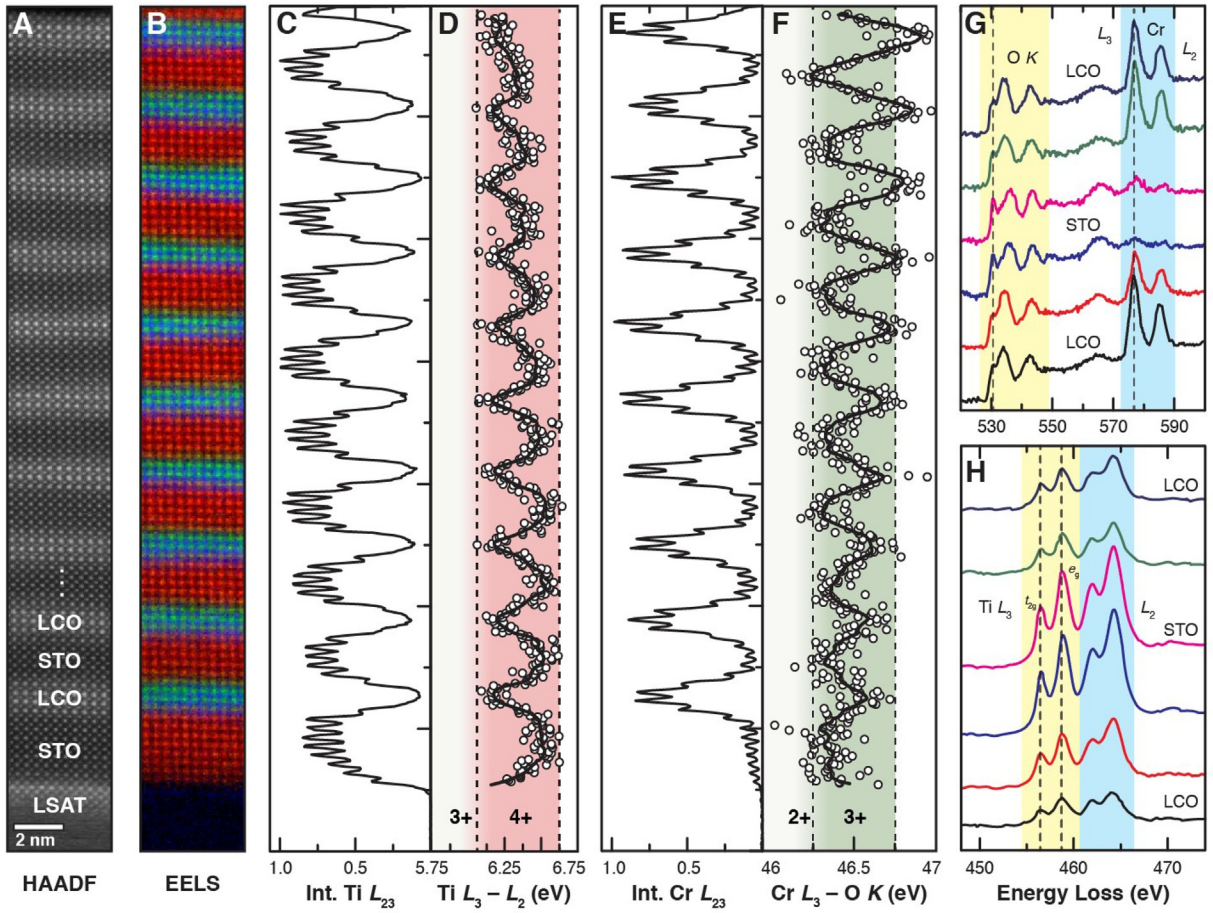

Fig. 1 STEM-EELS analysis of cation intermixing and defects. (A) Cross-sectional STEM-HAADF image of the superlattice acquired during EELS mapping. (B) Composition map of the Ti $L_{2,3}$, Cr $L_{2,3}$, and La $M_{4,5}$ (*red*, *green*, and *blue*, respectively) edges constructed using multiple linear least-squares fitting (MLLS). (C) Line profile of the integrated Ti $L_{2,3}$ edge intensity. (D) Line profile of the Ti L_3 and L_2 edge separation, used to estimate local Ti valence; this profile falls within the bounds of a Ti^{4+} state (marked by the dashed lines). (E) Line profile of the integrated Cr $L_{2,3}$ edge intensity. (F) Line profile of the O *K* and Cr L_3 edge energy loss separation, used to estimate local Cr valence; this profile falls within the bounds of a Cr^{3+} state (marked by the dashed lines). (G, H) O *K*/Cr $L_{2,3}$ and Ti $L_{2,3}$ edge spectra, respectively, extracted across the LCO/STO/LCO layers in the middle of the superlattice (*dashed lines* added as a guide to the eye). Reprinted with permission from Comes, R.B; Spurgeon, S. R.; Kepaptsoglou, D. M.; Engelhard, M. H.; Perea, D. E.; Kaspar, T. C.; Ramasse, Q. M.; Sushko, P. V.; Chambers, S. A. Probing the Origin of Interfacial Carriers in $SrTiO_3$ $LaCrO_3$ Superlattices. *Chem. Mater.* **2017,** *29*(3):1147–1155. Copyright 2017 American Chemical Society.

behavior of two or more phases at interfaces.[68] Composite structures based on $BaTiO_3$ (BTO) and PZT soon exhibited magnetoelectric coefficients orders of magnitude larger than in single-phase materials.[69]

A wide range of coupling mechanisms has been described in the literature, including charge screening, substrate-induced strain, and magnetic exchange.[59] Much previous work has focused on the presence of interface phases in these structures,[70,71] which are thought to mediate magnetoelectric coupling,[72,73] as well as interfacial magnetization through dead layer formation.[59,60,74–77] Particular attention has been paid to the LSMO/PZT system,[69] which combines the manganite's high ferromagnetic Curie temperature and spin polarization[78,79] with the large charge screening capabilities of the ferroelectric. Vaz *et al.* conducted the first in situ measurements of ultrathin LSMO on PZT using magnetooptical Kerr effect (MOKE) magnetometry, demonstrating coupling mediated by a bound layer of interace charge.[69,80–82] Metallic charge screening by Mn ions is thought to induce changes in the effective local Mn valence, modifying both magnetic moment and spin structure. While these early measurements provided important information about coupling, they were unable to directly probe the interface phases, chemistry, and spatial distribution of Mn valence—all essential parameters needed to develop more complete models of coupling.

Because of the challenges of poling TEM samples *in situ*, we developed an alternative substrate-induced self-poling technique.[83,84] This method takes advantage of the electrostatic boundary conditions of the substrate, which have been shown to induce spontaneous unidirectional polarization of PZT.[84–88] A ~2 nm $La_{0.7}Sr_{0.3}MnO_3$ buffer layer was first deposited on STO (001) using PLD, followed by a ~37 nm-thick $PbZr_{0.2}Ti_{0.8}O_3$ layer and a second ~19 nm-thick LSMO layer. This approach nominally produces two different interface charge states in a single sample, with the top layer in a hole charge depletion state and the bottom layer in an accumulation state.

STEM-EELS allows us to measure spatially resolved core loss spectra to probe local bonding and Mn valence, which we can then relate to the adjacent PZT polarization.[32,55,89] Fig. 2A shows a cross-sectional STEM-HAADF image of the heterostructure, overlaid with a line scan along which O *K* edge spectra were extracted in Fig. 2B. The fine structure of the edge arises from the first-order transition of electrons from the O 1*s* to 2*p* states; the three features labeled (A–C) are associated with hybridized states of O 2*p* states with Mn 3*d*, La 5*d*/Sr 4*d*, and Mn 4*sp* bands, respectively.[55] Clear shifts in the spectral weight and position of the fine structure features are evident across the LSMO/PZT interfaces, indicating local Mn valence changes. Fig. 2C shows the Mn $L_{2,3}$ edge, which has been aligned to the commonly used position of the O *K* edge near 532 eV[55]; the guides to the eye mark a distinct shift to lower L_3 energy onset in the vicinity of both interfaces, denoting a Mn valence reduction. While this procedure is not susceptible to energy drift errors, it is preferable to measure the absolute energy of the Mn $L_{2,3}$ edge relative to a known internal reference, such as the zero-loss peak or C *K* edge if possible, since the shape of the O *K* edge can change greatly depending on the compound.

Fig. 3A and B show plots of the O *K* pre- to main-peak energy separation ($\triangle E_{O(b-a)}$), which is independent of energy calibration. Both interfaces exhibit a decrease from a bulk value of 5.5–6 to <1.0 eV near the interface, but the bottom LSMO shows this drop over 1 nm versus 2.5–3 nm for the top interface. While these separations are in good qualitative agreement with standards investigated by Varela *et al.*,[55] direct, quantitative comparison to samples measured on other microscopes not advised because of differences in peak fitting and microscope parameters. Instead, we compare our values to DFT calculations to estimate the local variation in Mn doping; this, in turn, may be related to the bulk LSMO phase diagram to map the local phases present at both PZT interfaces. Fig. 3C and D shows the resulting spatially resolved LSMO phase diagram in the vicinity of the PZT. We find that the Mn valence corresponds to the expected bulk $La_{0.7}Sr_{0.3}MnO_3$ ($Mn^{3.3+}$) doping up to three lattice planes away from the bottom interface, where it drops by $\sim$0.15 over a nanometer. On the other hand, the top interface exhibits a larger $\sim$0.26 drop over a 2.5–3 nm region, indicating an asymmetric coupling. Comparison to the bulk LSMO phase diagram[90] shows that the bottom interface region is almost uniformly ferromagnetic and metallic to the PZT interface, while the top region transitions to a broad paramagnetic- insulating phase at the interface, which can explain the observed asymmetry. This behavior agrees quite well with a model that had been suggested for LSMO/BTO[91] but had never been applied to LSMO/PZT. These first-of-their-kind measurements of local phase gradients show that longer charge screening lengths can actually be the byproduct of an electrostatic doping-induced phase transition.

Interface Characterization of Fe_2O_3/Cr_2O_3 Heterostructures for Photocatalysis

In the "Cation Intermixing and Electronic Defects in LCO/STO Superlattices" section we discussed how STEM-EELS provides detailed insight into conductivity and the preservation of a built-in potential in photoactive superlatttices. Hemtatite (α-Fe_2O_3) is another system that has received considerable attention because of its abundance, stability, and suitable bandgap for photocatalysis.[92] Nanostructured hematite-based systems show promise for facilitating separation of electron–hole pairs, while enhancing the effective surface area available for photochemistry.[93] The superlattice layering of Fe_2O_3 with Cr_2O_3 has been shown to exhibit favorable band offset properties, leading to a sizable electrostatic potential, which can further improve the separation of electron–hole pairs.[94–96] However, to build and maintain this potential, we must strictly control layer termination, composition, and intermixing, which may be checked by the use of STEM probes, in conjunction with volume-averaged techniques.

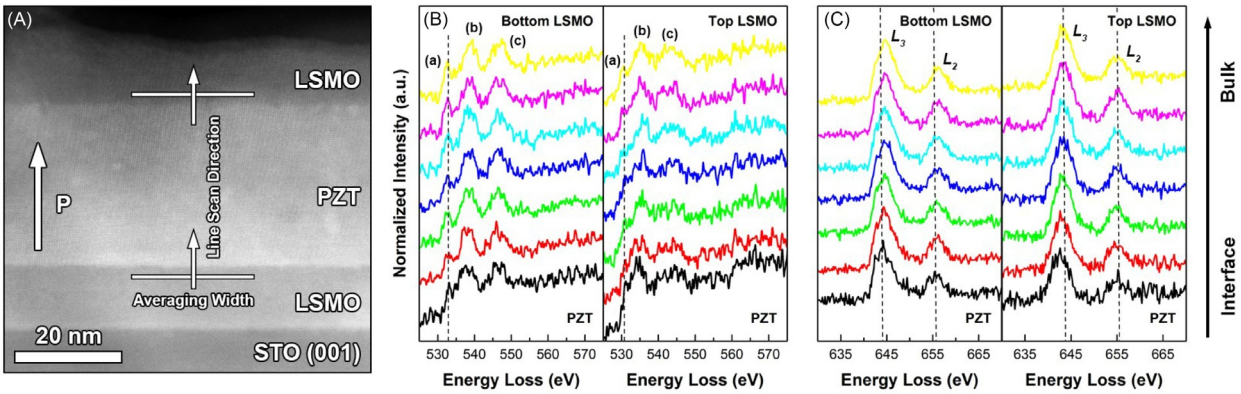

Fig. 2 Structural and chemical mapping of the heterostructure. (A) Cross-sectional STEM-HAADF image of the film structure, with the direction of ferroelectric polarization and linescan paths indicated. (B) Power-law subtracted EEL spectra corresponding to the O *K* edge, collected at every lattice plane beginning at the LSMO/PZT interface. (A), (B), and (C) correspond to the pre-, main-, and secondary-peak features, respectively. (C) Power-law subtracted EEL spectra corresponding to the Mn $L_{2,3}$ edge. Reprinted with permission from Spurgeon, S. R.; Balachandran, P. V.; Kepaptsoglou, D. M.; Damodaran, A.R.; Karthik, J.; Nejati, S.; Jones, L.; Ambaye, H.; Lauter, V.; Ramasse, Q. M.; Lau, K. K. S.; Martin, L. W.; Rondinelli, J. M.; Taheri, Mi-T. L. Polarization Screening-Induced Magnetic Phase Gradients at Complex Oxide Interfaces. *Nat. Commun.* **2015**, *6*, 6735. Copyright 2015. Rights managed by Nature Publishing Group.

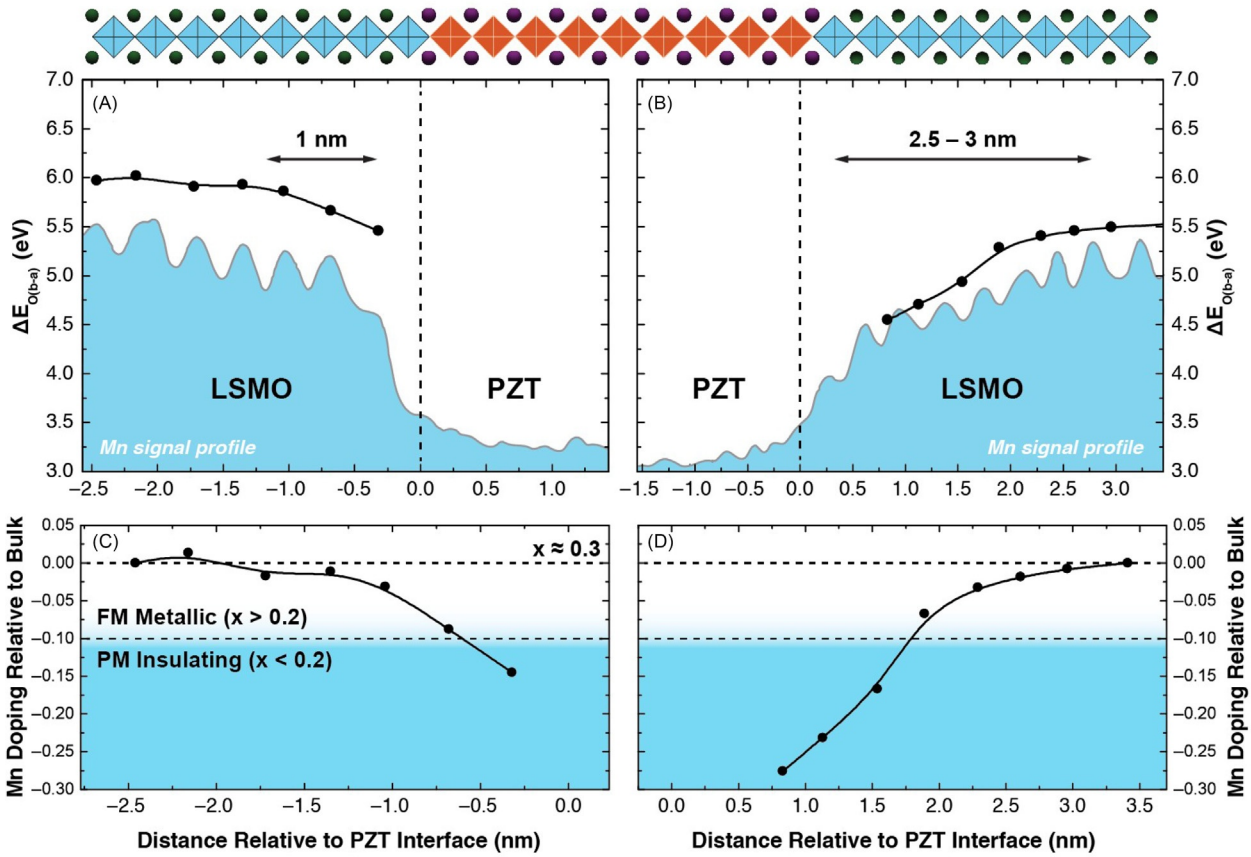

Fig. 3 Spatially resolved LSMO phase diagram. (A, B) show the O *K* pre- to main-peak separation ($\triangle E_{O(b-a)}$) in the vicinity of the PZT interface for the bottom and top LSMO layers, respectively, overlaid with an illustration of the heterostructure. (C, D) Map of local Mn doping relative to bulk LSMO as a function of position normal to the LSMO/PZT interface for the bottom (A) and top (B) LSMO layers. The marked boundaries of the associated magnetic and electronic phases are estimated from the bulk LSMO phase diagram.[90] Adapted with permission from Spurgeon, S. R.; Balachandran, P. V.; Kepaptsoglou, D. M.; Damodaran, A.R.; Karthik, J.; Nejati, S.; Jones, L.; Ambaye, H.; Lauter, V.; Ramasse, Q. M.; Lau, K. K. S.; Martin, L. W.; Rondinelli, J. M.; Taheri, Mi-T. L. Polarization Screening-Induced Magnetic Phase Gradients at Complex Oxide Interfaces. *Nat. Commun.* **2015**, *6*, 6735. Copyright 2015. Rights managed by Nature Publishing Group.

We have synthesized Fe_2O_3/Cr_2O_3 superlattices on Al_2O_3 (0001) substrates using MBE; careful control of the deposition ensures that each bilayer composition provides the largest conduction and valence band offsets, resulting in a large built-in electric field across the superlattice.[57] Fig. 4A shows a STEM-HAADF image of the overall film structure, inset with high magnification views of the film–substrate interface and superlattice. We observe that the interface with the Al_2O_3 substrate is coherent, uniform, and defect-free. Furthermore, all the layers of the superlattice are preserved, albeit with some undulation due to the large lattice mismatch of $a_{Cr_2O_3} - a_{Al_2O_3} / a_{Al_2O_3}$=4.2%. While the STEM-HAADF image shows a clear contrast between the film and substrate, the similar atomic number (Z) of the film layers necessitates the use of spectroscopy to directly resolve the superlattice components. Although STEM-EDS offers poorer energy resolution (~10 eV) than STEM-EELS (<0.1 eV), the technique is able to measure a wide range of ionization energies simultaneously, making it well-suited to the analysis of metal-oxides.[98] Fig. 4B shows a composite STEM-EDS map of the Al *K*, Fe *K*, and Cr *K* edges; this map confirms the overall composition and geometry of the film layers. For even more detail, we have acquired a STEM-EELS line scan from the HAADF image in Fig. 4C; by using a line scan (instead of a map) we are able to reduce the damage to the specimen, thereby preserving the integrity of the electronic fine structure. Fig. 4D shows the power law background-subtracted integrated Fe $L_{2,3}$, Cr $L_{2,3}$, and Ti $L_{2,3}$ edge signals, normalized to their concentration in the Cr_2O_3 buffer layer. The profile confirms the superlattice configuration in agreement with the STEM-EDS results, but the added spatial resolution shows that there is intermixing over ~0.5 nm near the bottom and top of the superlattice.

Turning to the electronic fine structure, we next explore systematic changes in the energy separation of the O *K* and Cr L_3 edges, as was done in "Cation Intermixing and Electronic Defects in LCO/STO Superlattices" section; using this approach, we avoid deconvolving the tail of the O edge from the onset of the Cr edge. Fig. 4E shows the measured energy separation, overlaid with range of values corresponding to a Cr^{3+}-like state extracted from the literature.[58] We observe a slight increase toward more Cr^{4+}-like character near the bottom of the superlattice, but the overall valence falls squarely within the bounds of the Cr^{3+}-like state; this behavior may reflect intermixing with the Fe layer, as is evident in Fig. 4C. To gain insight into the valence of the Fe, we have conducted measurements of the Fe$L_{2,3}$ white-line ratio according to the method of van Aken *et al.*,[97] as shown in Fig. 4F. Although

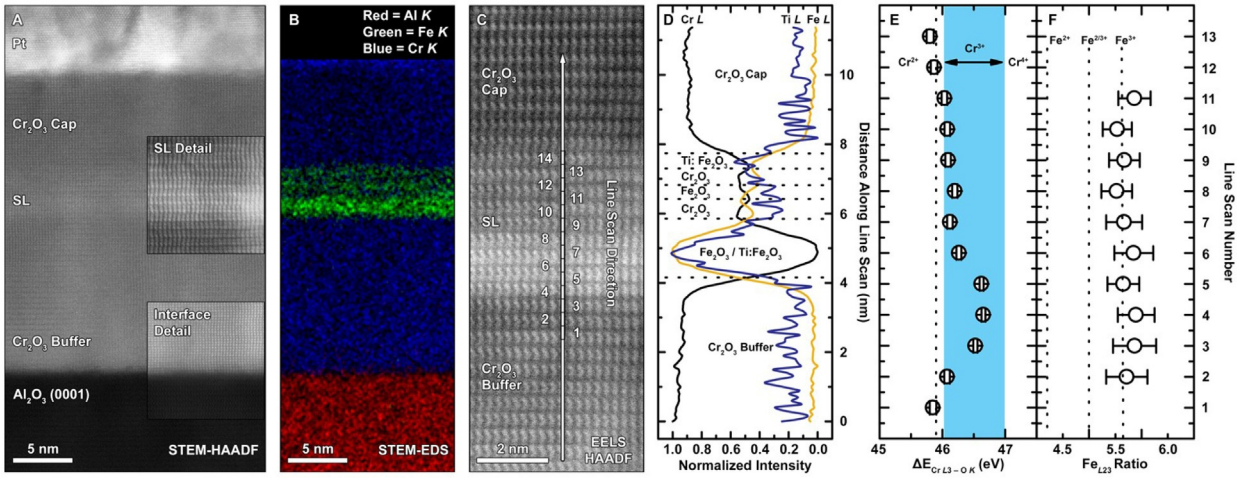

Fig. 4 STEM analysis of the Fe_2O_3/Cr_2O_3 superlattice. (A) Cross-sectional STEM-HAADF image of the film, inset with high magnification images of the film-substrate interface and superlattice. (B) STEM-EDS map of the Al *K*, Fe *K*, and Cr *K* peaks. (C) Radial-difference filtered STEM-HAADF image of the region used for EELS measurements. A line scan has been extracted and subsequent spectra have been integrated in the marked windows. (D) STEM-EELS integrated signal profiles extracted from the line scan region in C. The profiles were processed using principal component analysis, then background subtracted, and normalized to the Cr_2O_3 buffer layer. (E) O *K* and Cr L_3 edge energy loss separation, used to estimate local Cr valence; these points fall within the bounds of a Cr^{3+} state (marked by the *shaded region*). The error bars correspond to the standard error of Gaussian fits to the edge. (F) Fe $L_{2,3}$ white-line ratios calculated according to the method of van Aken *et al.*[97] The *dashed lines* correspond to the range of literature values. Reprinted with permission from Kaspar, T. C.; Schreiber, D. K.; Spurgeon, S. R.; McBriarty, M. E.; Carroll, G. M; Gamelin, D. R.; Chambers, S. A. Built-In Potential in Fe_2O_3-Cr_2O_3 Superlattices for Improved Photoexcited Carrier Separation. *Adv. Mater.* **2016**, *28*(8), 1616–1622. Copyright 2016 John Wiley and Sons.

we again emphasize that quantitative comparison to other results the literature is difficult, owing to differences in background subtraction and peak fitting methodologies, we find that the ratio falls within the range of values expected for an Fe^{3+}-like state.[97,99]

This study confirms that it is possible to synthesize high-quality Fe_2O_3/Cr_2O_3 superlattices using MBE. While STEM-EELS indicates some intermixing near the top and bottom of the superlattice, the overall chemistry of the Fe and Cr layers is preserved. In conjunction with XPS and related characterization,[57] we find that the favorable band alignment and enhanced photoconductivity of these materials may facilitate improved photoelectrochemical water splitting.

Challenges to Quantification of Atomic-Scale STEM-EDS Maps

As has been demonstrated in this article, chemical mapping using STEM-EELS and STEM-EDS offers several advantages compared to nonspectroscopic imaging. In particular, these techniques are directly sensitive to the elemental composition of a sample, whereas STEM-HAADF is less readily quantified. Furthermore, the enhanced energy resolution in EELS allows the operator to directly interrogate electronic fine structure and properties such as valence and bonding. However, strong interactions between the incident electron beam and lattice can lead to serious artifacts that preclude straightforward analysis of atomic-scale chemical maps. Effects such as beam broadening and channeling[38] are particularly troublesome along low-order zone axes, resulting in coupling between the probe and atomic columns.[35] Thermally scattered electrons can influence the ionization signal in both STEM-EDS and STEM-EELS,[36] as well as introduce image contrast reversals in STEM-EELS due to off-column probe channeling.[38,42] Although first-principles calculations have been able to model the Bremsstrahlung background in STEM-EDS,[98] resulting in a simpler signal integration process,[37] channeling and probe broadening through the specimen still make it difficult to accurately quantify unknown interfaces.[100]

To better understand sources of error in atomic-scale STEM-EDS mapping of interfaces, we have characterized a model heterostructure that shows potential use for a transparent, perovskite-based *p*–*n* junctions.[101] This system consists of a 30 nm-thick $La_{0.88}Sr_{0.12}CrO_3$ (*p*-type LSCO) thin-film deposited onto a 0.1 wt.% Nb:STO (001) (*n*-type Nb:STO) substrate using MBE.[102] The wedge-shaped sample shown in **Fig. 5** was prepared using a modified focused ion beam lift out procedure to produce a range of cross-section thicknesses. STEM-EDS maps were subsequently acquired from different regions spanning 28, 33, 50, 66, 70, and 75 nm-thick, according to zero-loss peak measurements.

Fig. 6A shows a representative cross-sectional STEM-HAADF image of the heterostructure. The sample displays excellent epitaxy between the film and substrate, with no obvious defects or misfit dislocations.[56] The contrast clearly changes across the film–substrate interface, resulting from the differing atomic numbers of the cation species, as well as a varying background contribution that is known to depend on sample thickness[103] and oxygen content. Even in the case of atomically abrupt interfaces, a finite sample thickness gives rise to an intermediate background different from either component of the junction.[103] While zero-loss

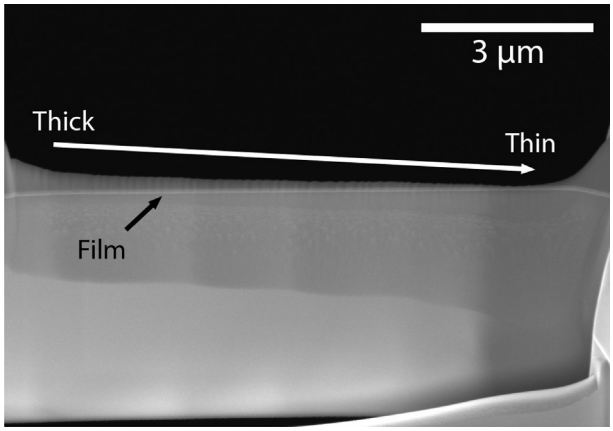

Fig. 5 STEM sample preparation. Cross-sectional secondary electron image of the polished lift out, with the gradient from thick to thin foil regions marked by the *arrow*. The bright horizontal band corresponds to the location of the film–substrate interface.

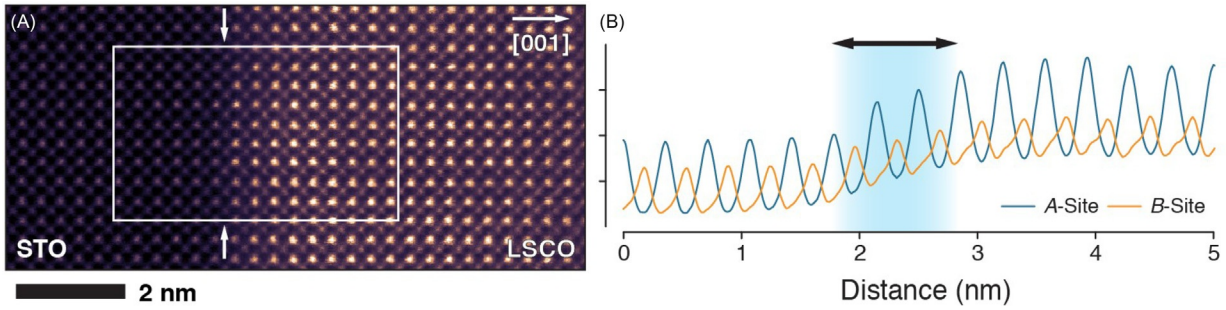

Fig. 6 LSCO/STO interface characterization. (A) Representative cross-sectional STEM-HAADF image of the LSCO/STO interface taken along the [100] zone-axis. (B) Average of 10 *A*- and *B*-site profiles taken across the interface, with the shaded region indicating the interface position.

measurements of the sample show minimal thickness fluctuations across the interface, we still observe a sloping background variation, as shown in the extracted line profile in Fig. 6B. Such a background hinders accurate quantification of intermixing, since it is possible to define the interface width in several ways: (1) relative to the changing background, (2) relative to the signal after background subtraction, or (3) relative to the column ratios within each layer.[104]

Since the cation species are similar in this compound, STEM-EDS can provide a more directly interpretable measurement of the interdiffusion of each species. Fig. 7A and B shows composite STEM-EDS maps and corresponding averaged line profiles for Sr L_α (1.806 kV), La L_α (4.650 kV), Ti K_α (4.508 kV), and Cr K_α (5.412 kV) edges taken from ~33 and ~75 nm-thick regions of the sample, respectively. We define the apparent interface width (δ) as the difference of 90% and 10% of the signal maxima from a logistic fit to either side of the interface. These profiles clearly reveal some intermixing, particularly of Ti and Cr, as we have observed in other samples.[54] Moreover, there are noticeable differences in the interface width between the two regions, as well as a higher background in the thicker part of the foil. We have repeated this same procedure for a range of foil thicknesses, as shown in Fig. 7C. We observe a clear trend toward more diffuse interfaces in thicker samples, ranging from 2–5 unit cells of artificial broadening depending on the species. We find that δ_{La} increases to ~1.8 nm moving from 28 to 75 nm-thick regions; similarly, δ_{Sr} and δ_{Cr} increase by ~0.86 and ~0.96 nm, respectively, while δ_{Ti} increases by ~0.87 nm. To confirm that these changes are not due to the presence of substrate steps, we have conducted atomic force microscope measurements of the STO surface prior to growth; our measurements show that at most only one step is present along the beam direction for the measured foil thicknesses, ruling out steps as a source of the artificial interface broadening. These results indicate that interface measurements strongly depend on sample preparation, as well as the choice of ionization edge, and that each exhibits different trends.

We have conducted multislice ionization simulations (described in reference 101) that confirm a consistent trend toward artificially broadened interfaces in thicker regions. We find that a foil thickness of only 40–50 nm is sufficient to introduce multiple unit cell measurement errors arising from complex beam channeling effects, as well as the delocalization character of each edge. We strongly recommend that rigorous sample preparation routines be employed to achieve the thinnest foils, with the best results being obtained below 25–30 nm. However, at these thicknesses it is difficult to achieve a reasonable ionization signal, necessitating the use of lower accelerating voltages (increasing the ionization cross-section), large-area EDS detectors, or advanced drift correction routines to enhance signal-to-noise.[105,106] Regardless, our results suggest that many atomically resolved maps may

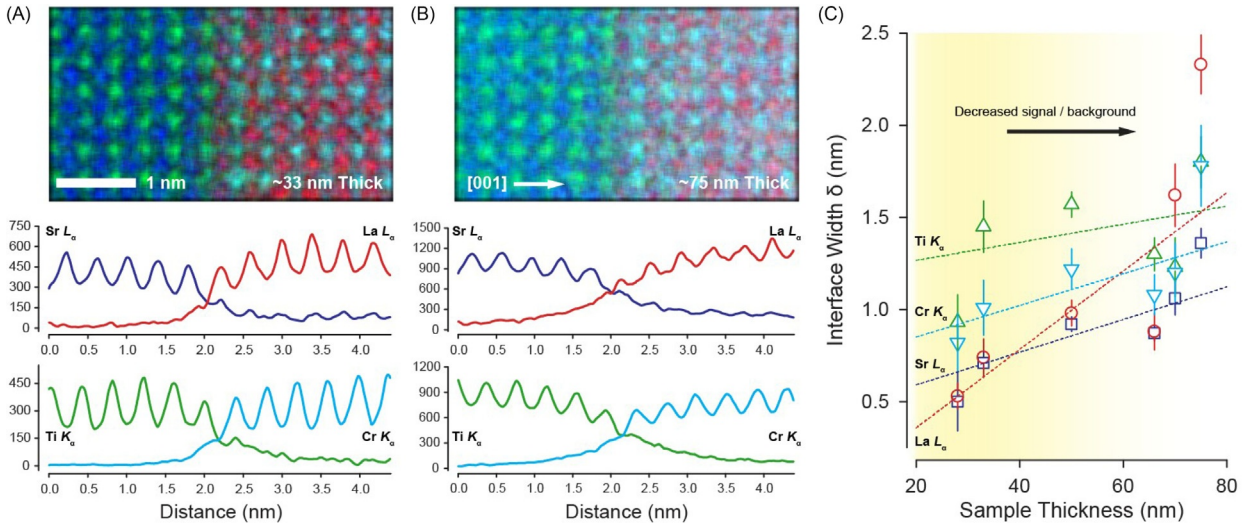

Fig. 7 Thickness dependence of STEM-EDS mapping. (A-B) Unfiltered composite STEM-EDS maps and corresponding *A*- and *B*-site net X-ray count line profiles for ~33 and ~75 nm-thick LSCO/STO interfaces, respectively. The line profiles have been averaged in the plane of the maps. (C) Interface width as a function of sample thickness for each species. Adapted with permission from Spurgeon, S. R.; Du, Y.; Chambers, S. A. Measurement Error in Atomic-Scale Scanning Transmission Electron Microscopy—Energy-Dispersive X-ray Spectroscopy (STEM- EDS) Mapping of a Model Oxide Interface. Microsc. Microanal. 2017, 23 (3), 513–517. Copyright 2017 Microscopy Society of America.

not be taken at face value and that accompanying theory calculations are needed to fully understand complex beam–specimen interactions.

Concluding Remarks

In this article we have illustrated the range of STEM techniques and their application to a variety of different oxide interfaces and superlattices. These techniques offer unparalleled spatial resolution and a panoply of structural, chemical, and compositional information that can greatly inform models for the behavior of oxides. While many of these methods are mature and well understood, there are still areas for improvement, particularly in the realm of image quantification and interpretation. Furthermore, we emphasize that STEM is often well complemented by other established techniques, such as X-ray diffraction and XPS, as well as emerging techniques, such as atom probe tomography, that can provide correlative volume-averaged information.[107,108] Using these tools we can develop a more complete and realistic understanding of functional interfaces needed to unlock next-generation materials and devices.

Acknowledgments

We would like to acknowledge all the contributors to this work, including Drs. Ryan Comes, Yingge Du, Tiffany Kaspar, Timothy Droubay, Peter Sushko, Phuong Vu Ong, Despoina Kepaptsoglou, Quentin Ramasse, Lewys Jones, Mitra Taheri, Prasanna Balachandran, Lane Martin, James Rondinelli, and many others. S.R.S. would like to thank Dr. Matthew Olszta for reviewing the article. The authors were supported by the U.S. Department of Energy (DOE), Basic Energy Sciences (BES), Division of Materials Sciences and Engineering under Award No. 10122. A portion of this work was performed in the Environmental Molecular Sciences Laboratory (EMSL), a national science user facility sponsored by the DOE Office of Biological and Environmental Research (BER) and located at Pacific Northwest National Laboratory (PNNL), operated for DOE by Battelle. Multislice calculations were performed using PNNL Institutional Computing.

References

1. Hawkes, P. W. The Correction of Electron Lens Aberrations. *Ultramicroscopy* **2015**, *156*, A1–A64.
2. Krivanek, O. L.; Corbin, G. J.; Dellby, N.; Elston, B. F.; Keyse, R. J.; Murfitt, M. F.; Own, C. S.; Szilagyi, Z. S.; Woodruff, J. W. An Electron Microscope for the Aberration-Corrected Era. *Ultramicroscopy* **2008**, *108* (3), 179–195.
3. Muller, D. A.; Fitting Kourkoutis, L.; Murfitt, M.; Song, J. H.; Hwang, H. Y.; Silcox, J.; Dellby, N.; Krivanek, O. L. Atomic-Scale Chemical Imaging of Composition and Bonding by Aberration- Corrected Microscopy. *Science* **2008**, *319* (5866), 1073–1076.

4. Bosman, M.; Keast, V. J.; García-Muñoz, J. L.; D'Alfonso, A. J.; Findlay, S. D.; Allen, L. J. Two-Dimensional Mapping of Chemical Information at Atomic Resolution. *Phys. Rev. Lett.* **2007**, *99* (8)086102.
5. Kimoto, K.; Asaka, T.; Nagai, T.; Saito, M.; Matsui, Y.; Ishizuka, K. Element-Selective Imaging of Atomic Columns in a Crystal Using STEM and EELS. *Nature* **2007**, *450* (7170), 702–704.
6. Varela, M.; Findlay, S. D.; Lupini, A. R.; Christen, H. M.; Borisevich, A. Y.; Dellby, N.; Krivanek, O. L.; Nellist, P. D.; Oxley, M. P.; Allen, L. J.; Pennycook, S. J. Spectroscopic Imaging of Single Atoms Within a Bulk Solid. *Phys. Rev. Lett.* **2004**, *92* (9)095502.
7. Batson, P. E.; Dellby, N.; Krivanek, O. L. Sub-Angstrom Resolution Using Aberration Corrected Electron Optics. *Nature* **2002**, *418* (6898), 617–620.
8. Batson, P. E. Simultaneous STEM Imaging and Electron Energy-Loss Spectroscopy With Atomic-Column Sensitivity. *Nature* **1993**, *366* (6457), 727–728.
9. Duscher, G.; Duscher, G.; Browning, N. D.; Pennycook, S. J. Atomic Column Resolved Electron Energy-Loss Spectroscopy. *Phys. Status Solid* **1998**, *166* (1), 327–342.
10. Browning, N. D.; Chisholm, M. F.; Pennycook, S. J. Atomic-Resolution Chemical Analysis Using a Scanning Transmission Electron Microscope. *Nature* **1993**, *366* (6451), 143–146.
11. Muller, D. A.; Tzou, Y.; Raj, R.; Silcox, J. Mapping sp^2 and sp^3 States of Carbon at sub-Nanometre Spatial Resolution. *Nature* **1993**, *366* (6457), 725–727.
12. Hwang, H. Y.; Iwasa, Y.; Kawasaki, M.; Keimer, B.; Nagaosa, N.; Tokura, Y. Emergent Phenomena at Oxide Interfaces. *Nat. Mater.* **2012**, *11* (2), 103–113.
13. Martin, L. W.; Chu, Y.-H.; Ramesh, R. Advances in the Growth and Characterization of Magnetic, Ferroelectric, and Multiferroic Oxide Thin Films. *Mat. Sci. Eng. R Rep.* **2010**, *68* (4–6), 89–133.
14. Ramesh, R.; Spaldin, N. A. Multiferroics: Progress and Prospects in Thin Films. *Nat. Mater.* **2007**, *6* (1), 21–29.
15. Chambers, S. A. Epitaxial Growth and Properties of Doped Transition Metal and Complex Oxide Films. *Adv. Mater.* **2010**, *22* (2), 219–248.
16. Chambers, S. A. Epitaxial Growth and Properties of Thin Film Oxides. *Surf. Sci. Rep.* **2000**, *39* (5–6), 105–180.
17. Egerton, R. F.; Li, P.; Malac, M. Radiation Damage in the TEM and SEM. *Micron* **2004**, *35* (6), 399–409.
18. de Groot, F.; Kotani, A. *Core Level Spectroscopy of Solids*; CRC Press: Advances in Condensed Matter Science, 2008.
19. Ootsuki, S.; Ikeno, H.; Umeda, Y.; Yonezawa, Y.; Moriwake, H.; Kuwabara, A.; Kido, O.; Ueda, S.; Tanaka, I.; Fujikawa, Y.; Zoguchi, F. M. Impact of Local Strain on Ti-$L_{2,3}$ Electron Energy-Loss Near-Edge Structures of $BaTiO_3$: A First-Principles Multiplet Study. *Microscopy* **2014**, *63* (3), 249–254.
20. Lopata, K.; Govind, N. Near and Above Ionization Electronic Excitations With non-Hermitian Real-Time Time-Dependent Density Functional Theory. *J. Chem. Theory Comput.* **2013**, *9* (11), 4939–4946.
21. Ootsuki, S.; Ikeno, H.; Umeda, Y.; Moriwake, H.; Kuwabara, A.; Kido, O.; Ueda, S.; Tanaka, I.; Fujikawa, Y.; Mizoguchi, T. Ab-Initio Multiplet Calculation of Oxygen Vacancy Effect on Ti- $L_{2,3}$ Electron Energy Loss Near Edge Structures of $BaTiO_3$. *Appl. Phys. Lett.* **2011**, *99* (23), 233109.
22. Allen, L. J. Simulation in Elemental Mapping Using Aberration-Corrected Electron Microscopy. *Ultramicroscopy* **2017**, *S0304–3991* (17), 30085–30092.
23. Allen, L. J.; D'Alfonso, A. J.; Findlay, S. D. Modelling the Inelastic Scattering of Fast Electrons. *Ultramicroscopy* **2015**, *151*, 11–22.
24. Kirkland, E. J. *Advanced Computing in Electron Microscopy*; Springer US: Boston, MA, 2010.
25. Cowley, J. M.; Moodie, A. F. The Scattering of Electrons by Atoms and Crystals. I. A New Theoretical Approach. *Acta Crystallogr.* **1957**, *10* (10), 609–619.
26. Gazquez, J.; Sanchez-Santolino, G.; Biskup, N.; Roldan, M. A.; Cabero, M.; Pennycook, S. J.; Varela, M. Applications of STEM-EELS to complex oxides. *Materials Science in Semiconductor Processing* **2017**, *65*, 49–63.
27. MacLaren, I.; Ramasse, Q. M. Aberration-Corrected Scanning Transmission Electron Microscopy for Atomic-Resolution Studies of Functional Oxides. *Int. Mater. Rev.* **2014**, *59* (3), 115–131.
28. Varela, M.; Lupini, A. R.; Van Benthem, K.; Borisevich, A. Y.; Chisholm, M. F.; Shibata, N.; Abe, E.; Pennycook, S. J. Materials Characterization in the Aberration-Corrected Scanning Transmission Electron Microscope. *Annu. Rev. Mat. Res.* **2005**, *35* (1), 539–569.
29. Chambers, S. A.; Engelhard, M. H.; Shutthanandan, V.; Zhu, Z.; Droubay, T. C.; Qiao, L.; Sushko, P. V.; Feng, T.; Lee, H. D.; Gustafsson, T.; Garfunkel, E.; Shah, A. B.; Zuo, J.-M.; Ramasse, Q. M. Instability, Intermixing and Electronic Structure at the Epitaxial $LaAlO_3/SrTiO_3$(001) Heterojunction. *Surf. Sci. Rep.* **2010**, *65* (10–12), 317–352.
30. Nakagawa, N.; Hwang, H. Y.; Muller, D. A. Why Some Interfaces Cannot be Sharp. *Nat. Mater.* **2006**, *5* (3), 204–209.
31. Cantoni, C.; Gazquez, J.; Granozio, F. M.; Oxley, M. P.; Varela, M.; Lupini, A. R.; Pennycook, S. J.; Aruta, C.; di Uccio, U. S.; Perna, P.; Maccariello, D. Electron Transfer and Ionic Displacements at the Origin of the 2D Electron Gas at the LAO/STO Interface: Direct Measurements With Atomic-Column Spatial Resolution. *Adv. Mater.* **2012**, *24* (29), 3952–3957.
32. Shah, A. B.; Ramasse, Q. M.; Zhai, X.; Wen, J. G.; May, S. J.; Petrov, I.; Bhattacharya, A.; Abbamonte, P.; Eckstein, J. N.; Zuo, J.-M. Probing Interfacial Electronic Structures in Atomic Layer $LaMnO_3$ and $SrTiO_3$ Superlattices. *Adv. Mater.* **2010**, *22* (10), 1156–1160.
33. Shah, A. B.; Ramasse, Q. M.; May, S. J.; Kavich, J.; Wen, J. G.; Zhai, X.; Eckstein, J. N.; Freeland, J.; Bhattacharya, A.; Zuo, J. M. Presence and Spatial Distribution of Interfacial Electronic States in $LaMnO_3$—$SrMnO_3$ Superlattices. *Phys. Rev. B* **2010**, *82* (11), 115112.
34. Kothleitner, G.; Neish, M. J.; Lugg, N. R.; Findlay, S. D.; Grogger, W.; Hofer, F.; Allen, L. J. Quantitative Elemental Mapping at Atomic Resolution Using X-Ray Spectroscopy. *Phys. Rev. Lett.* **2014**, *112* (8)085501.
35. Lugg, N. R.; Kothleitner, G.; Shibata, N.; Ikuhara, Y. On the Quantitativeness of EDS STEM. *Ultramicroscopy* **2014**, *151*, 150–159.
36. Forbes, B. D.; D'Alfonso, A. J.; Williams, R. E. A.; Srinivasan, R.; Fraser, H. L.; McComb, D. W.; Freitag, B.; Klenov, D. O.; Allen, L. J. Contribution of Thermally Scattered Electrons to Atomic Resolution Elemental Maps. *Phys. Rev. B* **2012**, *86* (2), 024108.
37. D'Alfonso, A. J.; Freitag, B.; Klenov, D.; Allen, L. J. Atomic-Resolution Chemical Mapping Using Energy-Dispersive X-Ray Spectroscopy. *Phys. Rev. B* **2010**, *81* (10), 100101.
38. Oxley, M. P.; Varela, M.; Pennycook, T. J.; van Benthem, K.; Findlay, S. D.; D'Alfonso,, A. J.; Allen, L. J.; Pennycook, S. J. Interpreting Atomic-Resolution Spectroscopic Images. *Phys. Rev. B* **2007**, *76* (6), 064303.
39. Findlay, S. D.; Oxley, M. P.; Pennycook, S. J.; Allen, L. J. Modelling Imaging Based on Core- Loss Spectroscopy in Scanning Transmission Electron Microscopy. *Ultramicroscopy* **2005**, *104* (2), 126–140.
40. Gulec, A.; Phillips, P. J.; Klie, R. F. Position-Sensitive Change in the Transition Metal *L*-Edge Fine Structures. *Appl. Phys. Lett.* **2015**, *107* (14), 143111.
41. Xin, H. L.; Dwyer, C.; Muller, D. A. Is There a Stobbs Factor in Atomic- Resolution STEM-EELS Mapping? *Ultramicroscopy* **2014**, *139*, 38–46.
42. Wang, P.; D'Alfonso,, A. J.; Findlay, S. D.; Allen, L. J.; Bleloch, A. L. Contrast Reversal in Atomic-Resolution Chemical Mapping. *Phys. Rev. Lett.* **2008**, *101* (23), 236102.
43. Dwyer, C.; Findlay, S. D.; Allen, L. J. Multiple Elastic Scattering of Core-Loss Electrons in Atomic Resolution Imaging. *Phys. Rev. B* **2008**, *77* (18), 184107.
44. Lu, P.; Xiong, J.; Van Benthem, M.; Jia, Q. Atomic-Scale Chemical Quantification of Oxide Interfaces Using Energy-Dispersive X-ray Spectroscopy. *Appl. Phys. Lett.* **2013**, *102* (17), 173111.
45. Lu, P.; Romero, E.; Lee, S.; MacManus-Driscoll, J. L.; Jia, Q. Chemical Quantification of Atomic-Scale EDS Maps Under Thin Specimen Conditions. *Microsc. Microanal.* **2014**, *20* (06), 1782–1790.
46. Neish, M. J.; Oxley, M. P.; Guo, J.; Sales, B. C.; Allen, L. J.; Chisholm, M. F. Local Observation of the Site Occupancy of Mn in a MnFePSi Compound. *Phys. Rev. Lett.* **2015**, *114* (10), 106101.
47. Mannhart, J.; Schlom, D. G. Oxide Interfaces–An Opportunity for Electronics. *Science* **2010**, *327* (5973), 1607–1611.
48. Schlom, D. G.; Chen, L.-Q.; Eom, C.-B.; Rabe, K. M.; Streiffer, S. K.; Triscone, J. M. Strain Tuning of Ferroelectric Thin Films. *Annu. Rev. Mat. Res.* **2007**, *37* (1), 589–626.
49. Ohtomo, A.; Hwang, H. Y. A High-Mobility Electron gas at the $LaAlO_3/SrTiO_3$ Heterointerface. *Nature* **2004**, *427* (6973), 423–426.
50. Qiao, L.; Droubay, T. C.; Varga, T.; Bowden, M. E.; Shutthanandan, V.; Zhu, Z.; Kaspar, T. C.; Chambers, S. A. Epitaxial Growth, Structure, and Intermixing at the $LaAlO_3/SrTiO_3$ Interface as the Film Stoichiometry is Varied. *Phys. Rev. B* **2011**, *83* (8), 085408.
51. Willmott, P.; Pauli, S.; Herger, R.; Schlepütz, C.; Martoccia, D.; Patterson, B.; Delley, B.; Clarke, R.; Kumah, D.; Cionca, C.; Yacoby, Y. Structural Basis for the Conducting Interface Between $LaAlO_3$ and $SrTiO_3$. *Phys. Rev. Lett.* **2007**, *99* (15), 155502.

52. Comes, R. B.; Spurgeon, S. R.; Heald, S. M.; Kepaptsoglou, D. M.; Jones, L.; Ong, P. V.; Bowden, M. E.; Ramasse, Q. M.; Sushko, P. V.; Chambers, S. A. Interface-Induced Polarization in $SrTiO_3$-$LaCrO_3$ Superlattices. *Adv. Mater. Interfaces* **2016**, *3* (10), 1500779.
53. Chambers, S. A.; Qiao, L.; Droubay, T. C.; Kaspar, T. C.; Arey, B. W.; Sushko, P. V. Band Alignment, Built-In Potential, and the Absence of Conductivity at the $LaCrO_3$/$SrTiO_3$ (001) Heterojunction. *Phys. Rev. Lett.* **2011**, *107* (20), 206802.
54. Comes, R. B.; Spurgeon, S. R.; Kepaptsoglou, D. M.; Engelhard, M. H.; Perea, D. E.; Kaspar, T. C.; Ramasse, Q. M.; Sushko, P. V.; Chambers, S. A. Probing the Origin of Interfacial Carriers in $SrTiO_3$ $LaCrO_3$ Superlattices. *Chem. Mater.* **2017**, *29* (3), 1147–1155.
55. Varela, M.; Oxley, M.; Luo, W.; Tao, J.; Watanabe, M.; Lupini, A.; Pantelides, S.; Pen-Nycook, S. Atomic-Resolution Imaging of Oxidation States in Manganites. *Phys. Rev. B* **2009**, *79* (8), 085117.
56. Colby, R.; Qiao, L.; Zhang, K. H. L.; Shutthanandan, V.; Ciston, J.; Kabius, B.; Chambers, S. A. Cation Intermixing and Electronic Deviations at the Insulating $LaCrO_3$/$SrTiO_3$(001) Interface. *Phys. Rev. B* **2013**, *88* (15), 155325.
57. Kaspar, T. C.; Schreiber, D. K.; Spurgeon, S. R.; McBriarty, M. E.; Carroll, G. E.; Gamelin, D. R.; Chambers, S. A. Built-In Potential in Fe_2O_3-Cr_2O_3 Superlattices for Improved Photoexcited Carrier Separation. *Adv. Mater.* **2016**, *28* (8), 1616–1622.
58. Arevalo-Lopez, A. M.; Alario-Franco, M. A. Reliable Method for Determining the Oxidation State in Chromium Oxides. *Inorg. Chem.* **2009**, *48* (24), 11843–11846.
59. Vaz, C. A. F.; Walker, F. J.; Ahn, C. H.; Ismail-Beigi, S. Intrinsic Interfacial Phenomena in Manganite Heterostructures. *J. Phys. Condens. Matter* **2015**, *27* (12), 123001.
60. Wang, Y.; Hu, J.; Lin, Y.; Nan, C. W. Multiferroic Magnetoelectric composite Nanostructures. *NPG Asia Mat.* **2010**, *2* (2), 61–68.
61. Wu, T.; Zurbuchen, M.; Saha, S.; Wang, R.-V.; Streiffer, S.; Mitchell, J. Observation of Magnetoelectric Effect in Epitaxial Ferroelectric Film/Manganite Crystal Heterostructures. *Phys. Rev. B* **2006**, *73* (13), 1–6.
62. Dorr, K.; Thiele, C. Multiferroic Bilayers of Manganites and Titanates. *Phys. Status Solidi* **2006**, *243* (1), 21–28.
63. Dagotto, E.; Hotta, T.; Moreo, A. Colossal Magnetoresistant Materials: The key Role of Phase Separation. *Phys. Rep.* **2001**, *344* (1–3), 1–153.
64. Coey, J. M. D.; Viret, M.; von Molnár, S. Mixed-Valence Manganites. *Adv. Physiol. Educ.* **1999**, *48* (2), 167–293.
65. Astrov, D. N. The Magnetoelectric Effect in Antiferromagnetic Materials. *Zhurnal Eksp. i Teor. Fiz.* **1960**, *38*, 984–985.
66. Fiebig, M. Revival of the Magnetoelectric Effect. *J. Phys. D Appl. Phys.* **2005**, *38* (8), R123–R152.
67. Catalan, G.; Scott, J. F. Physics and Applications of Bismuth Ferrite. *Adv. Mater.* **2009**, *21* (24), 2463–2485.
68. Srinivasan, G. Magnetoelectric Composites. *Annu. Rev. Mat. Res* **2010**, *40* (1), 153–178.
69. Vaz, C. A. F.; Hoffman, J.; Ahn, C. H.; Ramesh, R. Magnetoelectric Coupling Effects in Multiferroic Complex Oxide Composite Structures. *Adv. Mater.* **2010**, *22* (26–27), 2900–2918.
70. Valencia, S.; Peña, L.; Konstantinovic, Z.; Balcells, L.; Galceran, R.; Schmitz, D.; Sandiumenge, F.; Casanove, M.; Mart´ınez, B. Intrinsic Antiferromagnetic/Insulating Phase at Manganite Surfaces and Interfaces. *J. Phys. Condens. Matter* **2014**, *26* (16), 166001.
71. Huijben, M.; Martin, L. W.; Chu, Y.-H.; Holcomb, M. B.; Yu, P.; Rijnders, G.; Blank, D. H. A.; Ramesh, R. Critical Thickness and Orbital Ordering in Ultrathin $La_{0.7}Sr_{0.3}MnO_3$ Films. *Phys. Rev. B* **2008**, *78* (9), 1–7.
72. Dong, S.; Dagotto, E. Full Control of Magnetism in a Manganite Bilayer by Ferro-Electric Polarization. *Phys. Rev. B* **2013**, *88* (14), 140404.
73. Molegraaf, H. J. A.; Hoffman, J.; Vaz, C. A. F.; Gariglio, S.; van der Marel, D.; Ahn, C. H.; Triscone, J. M. Magnetoelectric Effects in Complex Oxides With Competing Ground States. *Adv. Mater.* **2009**, *21* (34), 3470–3474.
74. Jin, L.; Jia, C.-L.; Lindfors-Vrejoiu, I.; Zhong, X.; Du, H.; Dunin-Borkowski, R. E. Direct Demonstration of a Magnetic Dead Layer Resulting from A-Site Cation Inhomogeneity in a (La,Sr)MnO3 Epitaxial Film System. *Advanced Materials Interfaces* **2016**, *3* (18), 1600414.
75. Pradhan, K.; Kampf, A. P. Interfacial Magnetism in Manganite Superlattices. *Phys. Rev. B* **2013**, *88* (11)115136.
76. Luo, W.; Pennycook, S.; Pantelides, S. Magnetic Dead Layer at a Complex Oxide Interface. *Phys. Rev. Lett.* **2008**, *101* (24), 247204.
77. Sun, Y.; Zhao, Y.; Tian, H.; Xiong, C.; Xie, B.; Zhu, M.; Park, S.; Wu, W.; Li, J.; Li, Q. Electric and Magnetic Modulation of Fully Strained Dead Layers in $La_{0.67}Sr_{0.33}MnO_3$ Films. *Phys. Rev. B* **2008**, *78* (2), 024412.
78. Cesaria, M.; Caricato, A. P.; Maruccio, G.; Martino, M. LSMO Growing Opportunities by PLD and Applications in Spintronics. *J. Phys. Conf. Ser.* **2011**, *292*. 012003.
79. Moshnyaga, V.; Samwer, K. Ferromagnetic Manganite Films. In *Handbook of Magnetism and Advanced Magnetic Materials*; Kronmueller, H.; Parkin, S. S. P., Eds.; Wiley: Hoboken, 2003.
80. Vaz, C. A. F.; Hoffman, J.; Segal, Y.; Marshall, M. S. J.; Reiner, J. W.; Zhang, Z.; Grober, R. D.; Walker, F. J.; Ahn, C. H. Control of Magnetism in $Pb(Zr_{0.2}\ Ti_{0.8})O_3/La_{0.8}\ Sr_{0.2}\ MnO_3$ Multiferroic Heterostructures. *J. Appl. Phys.* **2011**, *109* (7), 07D905.
81. Vaz, C. A. F.; Hoffman, J.; Segal, Y.; Reiner, J. W.; Grober, R. D.; Zhang, Z.; Ahn, C. H.; Walker, F. J. Origin of the Magnetoelectric Coupling Effect in $Pb(Zr_{0.2}\ Ti_{0.8})O_3/La_{0.8}\ Sr_{0.2}$ MnO_3 Multiferroic Heterostructures. *Phys. Rev. Lett.* **2010**, *104* (12), 127202.
82. Vaz, C. A. F.; Segal, Y.; Hoffman, J.; Grober, R. D.; Walker, F. J.; Ahn, C. H. Tempera- Ture Dependence of the Magnetoelectric Effect in $Pb(Zr_{0.2}Ti_{0.8})O_3/La_{0.8}Sr_{0.2}MnO_3$ Multiferroic Heterostructures. *Appl. Phys. Lett.* **2010**, *97* (4), 042506.
83. Spurgeon, S. R.; Balachandran, P. V.; Kepaptsoglou, D. M.; Damodaran, A. R.; Karthik, J.; Nejati, S.; Jones, L.; Ambaye, H.; Lauter, V.; Ramasse, Q. M.; Lau, K. K. S.; Martin, L. W.; Rondinelli, J. M.; Taheri, M. T. L. Polarization Screening-Induced Magnetic Phase Gradients at Complex Oxide Interfaces. *Nat. Commun.* **2015**, *6*, 6735.
84. Yu, P.; Luo, W.; Yi, D.; Zhang, J. X.; Rossell, M. D.; Yang, C.-H.; You, L.; Singh-Bhalla, G.; Yang, S. Y.; He, Q.; Ramasse, Q. M.; Erni, R.; Martin, L. W.; Chu, Y. H.; Pantelides, S. T.; Pennycook, S. J.; Ramesh, R. Interface Control of Bulk Ferroelectric Polarization. *Proc. Natl. Acad. Sci. U. S. A.* **2012**, *109* (25), 9710–9715.
85. Spurgeon, S. R.; Sloppy, J. D.; Kepaptsoglou, D. M.; Balachandran, P. V.; Nejati, S.; Karthik, J.; Damodaran, A. R.; Johnson, C. L.; Ambaye, H.; Goyette, R.; Lauter, V.; Ramasse, Q. M.; Idrobo, J. C.; Lau, K. K. S.; Lofland, S. E.; Rondinelli, J. M.; Martin, L. W.; Taheri, M. L. Thickness-Dependent Crossover from Charge- to Strain-Mediated Magnetoelectric Coupling in Ferromagnetic/Piezoelectric Oxide Heterostructures. *ACS Nano* **2014**, *8* (1), 894–903.
86. Chen, J.; Lu, H.; Liu, H.-J.; Chu, Y.-H.; Dunn, S.; Ostrikov, K. K.; Gruverman, A.; Valanoor, N. Interface Control of Surface Photochemical Reactivity in Ultrathin Epitaxial Ferroelectric Films. *Appl. Phys. Lett.* **2013**, *102* (18), 182904.
87. Karthik, J.; Damodaran, A. R.; Martin, L. W. Epitaxial Ferroelectric Heterostructures Fabricated by Selective Area Epitaxy of $SrRuO_3$ Using an MgO Mask. *Adv. Mater.* **2012**, *24* (12), 1610–1615.
88. Afanasjev, V. P.; Petrov, A. A.; Pronin, I. P.; Tarakanov, E. A.; Kaptelov, E. J.; Graul, J. Polarization and Self-Polarization in Thin $PbZr_{1-x}\ Ti_xO_3$ (PZT) Films. *J. Phys. Condens. Matter* **2001**, *13* (39), 8755–8763.
89. Tan, H.; Verbeeck, J.; Abakumov, A.; Van Tendeloo, G. Oxidation state and chemical shift investigation in transition metal oxides by EELS. *Ultramicroscopy* **2012**, *116*, 24–33.
90. Zubko, P.; Gariglio, S.; Gabay, M.; Ghosez, P.; Triscone, J. M. In- terface Physics in Complex Oxide Heterostructures. *Annu. Rev. Condens. Matter Phys.* **2011**, *2* (1), 141–165.
91. Lu, H.; George, T. A.; Wang, Y.; Ketsman, I.; Burton, J. D.; Bark, C.-W.; Ryu, S.; Kim, D. J.; Wang, J.; Binek, C.; Dowben, P. A.; Sokolov, A.; Eom, C.-B.; Tsymbal, E. Y.; Gruverman, A. Electric Modulation of Magnetization at the $BaTiO_3/La_{0.67}Sr_{0.33}MnO_3$ Interfaces. *Appl. Phys. Lett.* **2012**, *100* (23), 232904.
92. Shen, S. Toward Efficient Solar Water Splitting Over Hematite Photoelectrodes. *J. Mat. Res.* **2014**, *29* (01), 29–46.
93. Kay, A.; Cesar, I.; Gra¨tzel, M. New Benchmark for Water Photooxidation by Nanostructured α-Fe_2O_3 Films. *J. Am. Chem. Soc.* **2006**, *128* (49), 15714–15721.
94. Kaspar, T. C.; Chamberlin, S. E.; Chambers, S. A. Surface Structure of α- Cr_2O_3(0001) After Activated Oxygen Exposure. *Surf. Sci.* **2013**, *618*, 159–166.
95. Chambers, S. A.; Liang, Y.; Gao, Y. Noncummutative Band Offset at α-Cr_2O_3/α-Fe_2O_3 (0001) Heterojunctions. *Phys. Rev. B* **2000**, *61* (19), 13223–13229.
96. Chambers, S. A.; Yi, S. I. Fe Termination for α-Fe_2O_3(0001) as Grown by Oxygen-Plasma-Assisted Molecular Beam Epitaxy. *Surf. Sci.* **1999**, *439* (1-3), L785–L791.
97. Van Aken, P. A.; Liebscher, B. Quantification of Ferrous/Ferric Ratios in Minerals: New Evaluation Schemes of Fe L_{23} Electron Energy-Loss Near-Edge Spectra. *Phys. Chem. Miner.* **2002**, *29*, 188–200.
98. Williams, D. B.; Carter, C. B. *Transmission Electron Microscopy*; Springer: Berlin, 2009.

99. Cavé, L.; Al, T.; Loomer, D.; Cogswell, S.; Weaver, L. A STEM/EELS Method for Mapping Iron Valence Ratios in Oxide Minerals. *Micron* **2006**, *37* (4), 301–309.
100. Kotula, P. G.; Klenov, D. O.; von Harrach, H. S. Challenges to Quantitative Multivariate Statistical Analysis of Atomic-Resolution X-Ray Spectra. *Microsc. Microanal.* **2012**, *18* (04), 691–698.
101. Spurgeon, S. R.; Du, Y.; Chambers, S. A. Measurement Error in Atomic-Scale Scanning Transmission Electron Microscopy—Energy-Dispersive X-ray Spectroscopy (STEM-EDS) Mapping of a Model Oxide Interface. *Microsc. Microanal.* **2017**, *23* (3), 513–517.
102. Zhang, K. H. L.; Du, Y.; Papadogianni, A.; Bierwagen, O.; Sallis, S.; Piper, L. F. J.; Bowden, M. E.; Shutthanandan, V.; Sushko, P. V.; Chambers, S. A. Perovskite Sr-Doped $LaCrO_3$ as a New *p*-Type Transparent Conducting Oxide. *Adv. Mater.* **2015**, *27* (35), 5191–5195.
103. Klenov, O. D.; Stemmer, S. Contributions to the Contrast in Experimental High-Angle Annular Dark-Field Images. *Ultramicroscopy* **2006**, *106* (10), 889–901.
104. Robb, P. D.; Finnie, M.; Longo, P.; Craven, A. J. Experimental Evaluation of Interfaces Using Atomic-Resolution High Angle Annular Dark Field (HAADF) Imaging. *Ultramicroscopy* **2012**, *114*, 11–19.
105. Wenner, S.; Jones, L.; Marioara, C. D.; Holmestad, R. Atomic-Resolution Chemical Mapping of Ordered Precipitates in Al Alloys Using Energy-Dispersive X-Ray Spectroscopy. *Micron* **2017**, *96*, 103–111.
106. Jones, L.; Yang, H.; Pennycook, T. J.; Marshall, M. S. J.; Van Aert, S.; Browning, N. D.; Castell, M. R.; Nellist, P. D. Smart Align: A New Tool for Robust Non-Rigid Registration of Scanning Microscope Data. *Adv. Struct. Chem. Imaging* **2015**, *1* (1), 8.
107. Spurgeon, S. R.; Du, Y.; Droubay, T.; Devaraj, A.; Sang, X.; Longo, P.; Yan, P.; Kotula, P. G.; Shutthanandan, V.; Bowden, M. E.; LeBeau, J. M.; Wang, C.; Sushko, P. V.; Chambers, S. A. Competing Pathways for Nucleation of the Double Perovskite Structure in the Epitaxial Synthesis of La_2MnNiO_6. *Chem. Mater.* **2016**, *28* (11), 3814–3822.
108. Comes, R. B.; Perea, D. E.; Spurgeon, S. R. *Heterogeneous Two-Phase Pillars in Epitaxial NiF_2O_4 - $LaFeO_3$ Nanocomposites*; Adv. Mater: Int, 2017;http://dx.doi.org/10.1002/admi.201700396 In press.
109. Egerton, R. F. *Electron Energy-Loss Spectroscopy in the Electron Microscope*; Springer: New York, 2012.
110. Allen, L. J.; D'Alfonso, A. J.; Freitag, B.; Klenov, D. O. Chemical Mapping at Atomic Resolution Using Energy-Dispersive X-Ray Spectroscopy. *MRS Bull.* **2012**, *37* (01), 47–52.
111. Egerton, R. F. Electron Energy-Loss Spectroscopy in the TEM. *Rep. Prog. Phys.* **2009**, *72* (1), 016502.

Further Reading

Egerton, R. F. *Electron Energy-Loss Spectroscopy in the Electron Microscope*; Springer US: Boston, MA, 2012.

Allen, L.J. Simulation in elemental mapping using aberration-corrected electron microscopy. *Ultramicroscopy* **2017**.

Gázquez, J., Sánchez-Santolino, G., Biškup, N., Roldán, M. A., Cabero, M., Pennycook, S. J., and Varela, M. 2016. Applications of STEM-EELS to complex oxides. *Mater. Sci. Semicond. Process*. In press.

Egerton, R. F. Electron Energy-Loss Spectroscopy in the TEM. *Reports Prog. Phys.* **2009**, *72* (1), 016502.